RSC Advances

PAPER

View Article Online
View Journal | View Issue

Cite this: *RSC Adv.*, 2026, **16**, 14477

Joint removal of pollutants from sulfide ore flotation wastewater using composite oily sludge-based adsorbents

Peng Fu, [a] Huifen Yang*[a] and Jingwen Zhao[b]

This study explores a sustainable "waste-treating-waste" strategy by synthesizing two distinct adsorbents, tank-bottom oily sludge adsorption material (TSAM) and refinery oily sludge adsorption material (RSAM). These materials are produced by pyrolysis at 800 °C and applied to the removal of complex sulfide ore flotation wastewater. Characterization results revealed that RSAM possesses a superior surface area (204 m^2 g^{-1}) and a well-developed mesoporous structure, providing abundant active sites for organic molecules. In contrast, TSAM is characterized by a higher ash content and the presence of active mineral phases, such as CaS and FeS, which play a crucial role in heavy metal pollutant immobilization. Adsorption experiments demonstrated distinct but complementary performance: RSAM exhibited exceptional removal efficiency for butyl xanthate (BX), achieving 99.60% removal within 45 minutes, a process primarily driven by physical mechanisms, including pore filling within the carbon matrix and strong hydrophobic interactions between the adsorbent surface and xanthate. Conversely, TSAM showed superior efficacy in removing heavy metal ions (Cd^{2+}, Cu^{2+}, Zn^{2+}) with removal efficiencies exceeding 97%. The removal of heavy metals by TSAM was governed by combined chemical mechanisms, involving chemical precipitation (forming stable metal sulfides and carbonates), surface complexation with oxygen-containing functional groups, and ion exchange, further facilitated by the material's strong alkaline-buffering capacity. The treatment of actual flotation wastewater demonstrated that pollutant levels were significantly below discharge limits. This research provides a cost-effective solution for the simultaneous removal of organic and heavy metal pollutants, demonstrating the high-value valorization of petroleum hazardous waste within a circular economy framework.

Received 21st January 2026
Accepted 11th March 2026

DOI: 10.1039/d6ra00534a

rsc.li/rsc-advances

1 Introduction

Oily sludge, recognized as one of the most hazardous solid wastes from the petroleum industry, poses significant environmental challenges due to its substantial production volume and complex composition. Global estimates indicate that refineries produce approximately 190 000 m^3 of oily sludge daily.[1] In China alone, annual production exceeds 6 million tons, with historical stockpiles reaching 143 million tons.[2] Physicochemically, oily sludge is a stable emulsified system containing toxic components such as polycyclic aromatic hydrocarbons (PAHs), BTEX(benzene, toluene, ethylbenzene, xylenes), and heavy metals.[3] While its hazardous nature complicates treatment, the high content of carbonaceous organic matter and inorganic solids positions oily sludge as a potential precursor for carbon-based materials.

To mitigate the environmental risks and reduce the volume of oily sludge, various treatment technologies have been employed, including solvent extraction, incineration, biodegradation, and landfilling.[4] However, the widespread implementation of these conventional methods is often constrained by secondary pollution or economic inefficiencies. For instance, incineration, while effective for volume reduction, poses risks of releasing toxic gases and requires high energy input. Biological treatments are environmentally friendly but are often inhibited by the high toxicity of heavy metals and require long processing cycles. In contrast, pyrolysis technology has garnered increasing attention as a sustainable thermochemical conversion route. By treating sludge in an oxygen-limited environment, pyrolysis not only effectively recovers valuable fuel oil and minimizes waste volume but also immobilizes heavy metals. Crucially, this process converts the organic-rich solid phase into a stable carbonaceous residue, creating a pivotal opportunity for transforming hazardous waste into functional materials.[5]

The high content of carbonaceous organic matter and solid inorganic components in oily sludge positions it as a premier candidate for the production of functional carbon-based adsorbents. Pyrolysis represents an exceptionally effective

[a]*School of Resources and Safety Engineer, University of Science and Technology Beijing, 30 Xueyuan Road, Haidian District, Beijing 100083, China. E-mail: 358756757@qq.com*

[b]*School of Mining and Coal Engineering, Inner Mongolia University of Science and Technology, Baotou 014010, China*

thermochemical route for this valorization, converting the complex petroleum hydrocarbons—including saturates, aromatics, resins, and asphaltenes—into stable pyrogenic chars with developed pore structures and rich surface functional groups.[6]

Recent research has demonstrated that these oily sludge-derived residues can be precisely engineered into high-performance materials through chemical activation.[7,8] Gong *et al.*[9] successfully prepared nitrogen-doped porous carbon by treating oily sludge pyrolysis residues with KOH and urea, achieving a superior specific surface area (1224 $m^2\ g^{-1}$) and a large pore volume (1.7 $cm^3\ g^{-1}$). These structural enhancements resulted in excellent CO_2 adsorption capacity and regeneration stability. Furthermore, the application of Porous Carbonaceous Solid Waste (PCSW) derived from tank-bottom oily sludge exemplifies the "waste-treating-waste" strategy. Studies on arsenic-laden leachate from lead smelting demonstrated that PCSW could achieve an arsenic removal efficiency of 96.26%, with a maximum adsorption capacity of 45.314 mg g^{-1}.[10] Notably, PCSW also showed remarkable capability for the simultaneous removal of other heavy metals, such as Pb, Zn, Cu and Cd, reducing their residual concentrations below national emission standards without the need for additional chemical modification.

The technical and economic feasibility of this strategy is further supported by extensive literature on municipal sewage sludge. Extensive studies have confirmed that sludge-derived biochar, produced by pyrolysis (350–950 °C) and chemical activation (*e.g.*, $ZnCl_2$, KOH), can remove a diverse range of pollutants including Cu^{2+}, Cd^{2+}, and antibiotics.[11–15] Innovative modifications, such as catalytic pyrolysis with pyrolusite or co-pyrolysis with fly ash, have been shown to increase specific surface area and surface functional groups, yielding removal efficiencies exceeding 99% for certain heavy metals.[16,17] Importantly, the production cost of these sludge-based adsorbents is estimated to be only 5–10% of commercial activated carbon.[12] By adapting these established activation strategies to oily sludge, it is possible to transform this hazardous refinery byproduct into a robust, cost-effective adsorbent tailored for complex industrial wastewater remediation.

Mineral processing effluents are a major contributor to mining water pollution, characterized by a highly complex matrix containing both inorganic heavy metals and organic flotation reagents. Heavy metals, such as Cd, Cr, Cu, Ni, As, Pb, and Zn, pose severe threats to human health and aquatic ecosystems due to their high solubility, persistence, and non-biodegradability. These carcinogens readily enter the food chain through leaching and biomagnification, ultimately inhibiting essential cellular processes such as DNA replication and cell division.[18–21] Chronic exposure is linked to severe pathologies, including organ damage and nervous system impairment.[22–24] Simultaneously, these streams contain significant concentrations of residual organic flotation reagents, particularly xanthates. Residual xanthates pose a severe threat through direct toxicity, impairing planktonic algae and zooplankton at concentrations as low as 2.0–10.0 mg L^{-1}.[25] Furthermore, they can hydrolyze into carbon disulfide (CS_2), a neurotoxic compound that causes fish mortality at 5.0 mg L^{-1} within days.[26,27] Beyond environmental toxicity, residual xanthates interfere with flotation selectivity during water recycling, complicating the mineral recovery process.[28]

To mitigate these risks, various technologies have been developed for industrial wastewater treatment. Conventional methods for heavy metal removal, such as coagulation/flocculation, chemical precipitation, and electrochemical technologies, are widely applied due to their established infrastructure.[29–31] However, large-scale implementation reveals significant deficiencies, including low removal efficiencies in acidic environments and substantial secondary sludge generation.[32] For the organic fraction, several advanced oxidation processes (AOPs), such as TiO_2-based photocatalysis, Fenton-like processes, and ozone oxidation, have proven effective for xanthate degradation, often achieving efficiencies exceeding 90%.[33–35] Nevertheless, the industrial application of AOPs faces practical hurdles, including high operational costs, potential catalyst deactivation, and extreme sensitivity to the complex matrices of real mining wastewater. While advanced techniques like membrane filtration offer improved performance for both pollutant types, their high operational complexity and costs limit their widespread adoption in resource-intensive sectors like mining.[36,37]

There is an urgent need for highly efficient, low-cost, and robust alternatives, which has shifted research focus toward sustainable adsorption materials. Compared to conventional treatments, adsorption has emerged as a cost-effective and versatile strategy, particularly advantageous for large-scale mining applications due to its operational simplicity and ability to simultaneously capture organic reagents and heavy metal ions.[38,39] To date, various material classes have shown promise, including modified natural minerals,[40] magnetic composites,[41] and biological materials.[42,43] Valorizing industrial by-products like fly ash also aligns with circular economy principles by reducing waste while providing functional materials.[44] In this study, two distinct carbonaceous adsorbents were synthesized by pyrolysis of tank-bottom oily sludge and refinery oily sludge, respectively. Compared with relevant previous studies, the present work achieves the simultaneous removal of heavy metals and xanthate organic reagents from real mineral processing flotation wastewater by using sludge-derived carbon adsorbents, which further extends the application boundary of oily sludge-based materials. The physicochemical properties and pore structures of these sludge-derived materials were systematically characterized to evaluate their potential for treating complex sulfide ore flotation effluents. This work establishes a cost-effective "waste-treating-waste" strategy for both oily sludge valorization and multi-pollutant wastewater treatment.

2 Materials and methods

2.1 Preparation of TSAM and RSAM

Tank bottom oily sludge adsorption materials (TSAM) and refinery oily sludge adsorption materials (RSAM) were prepared according to the method described by Fu *et al.* and Yang

et al.,[45,46] separately. Tank bottom oily sludge and refinery oily sludge are the waste from refinery plant of Sinopec Yanshan Petrochemical Co. (Beijing, China). The Weigh a certain amount of oily sludge, put them into a corundum crucible and placed into the tubular furnace. Tank bottom oily sludge was heated up to 800 °C at the heating rate of 10 °C min^{-1}, the N_2 flow was 140 mL min^{-1}, pyrolysis time was 75 min. The residues solid in crucible was grounded to 0.15 mm and was named as tank bottom oily sludge adsorption materials-TSAM. Refinery oily sludge was heated up to 800 °C at the heating rate of 8 °C min^{-1}, the N_2 flow was 140 mL min^{-1}, pyrolysis time was 45 min. The residues solid in crucible was grounded to 0.15 mm and was named as refinery oily sludge adsorption materials-RSAM.

2.2 Characterization and analytical methods

Proximate analysis was conducted in accordance with the standard method for proximate analysis of coal (GB/T 212-2008), the ultimate analysis was performed using X-ray fluorescence spectrometry (XRF). A BRUKER D-8 X-ray diffraction analyzer with Cu Kα radiation to detect the phase of TSAM and RSAM. The tube voltage was 40 kV, the maximum tube current was 100 mA, and the scanning range was 10 to 90° with the scanning rate of 5°/min. N_2 sorption isotherms were measured at 77 K with Quantachrome Instruments Autosorb IQ. The specific surface areas were calculated by the Brunauer–Emmett–Teller (BET) methods, and the pore size distributions and pore volumes were calculated by Barrett–Joyner–Halenda (BJH) models. The morphology and microstructure were studied by ZEISS SUPRA 55 scanning electron microscopes (SEM), and composition were analyzed by the coupled OXFORD X-Max 20 energy-dispersive spectrometer (EDS). The elemental, chemical state, and molecular information from the surfaces of solid materials were detected by Time-of-Flight Secondary Ion Mass Spectrometry (TOF. SIMS 5 IONTOF GmbH), the primary ion beam was 30 kV Bi_3^+ in a static mode with an analysis current of 10 pA. The calibration was performed in the positive secondary ion mass spectra using the signal for C^+, CH_3^+ at the *m*/*z* of 12 and 15.01, *etc.* The chemical state of the element is determined by X-ray Photoelectron Spectroscopy (XPS, Thermo Fisher Scientific K-Alpha Microprobe, USA).

Toxicity leaching tests were performed following solid waste-extraction procedure for leaching toxicity-sulphuric acid & nitric acid method HJ/T 299-2007 and solid waste-extraction procedure for leaching toxicity-horizontal vibration method HJ 557-2010 to assess the environmental safety of adsorbent materials. Nitric/sulfuric acid and deionized water were used as leachants to simulate acidic and surface water conditions. Samples (100 g dry weight) were mixed with leachant (10 : 1 L kg^{-1}) in 2 L bottles and agitated at 30 ± 2 rpm for 8 h, followed by 16 h settling. The filtered (0.45 μm) eluates were analyzed by ICP-MS and AAS.

2.3 General batch adsorption procedure

2.3.1 Batch adsorption study. The adsorption performance of TSAM and RSAM was investigated through batch adsorption experiments. Prior to the experiments, stock solutions of butyl xanthate and metal ions (Cd^{2+}, Cu^{2+}, and Zn^{2+}) were prepared by dissolving precise quantities of butyl xanthate, $Cd(SO_4)_2$, $Cu(SO_4)_2$, and $Zn(NO_3)_2 \cdot 6H_2O$ in deionized water. The pH of each solution was adjusted using 0.1 M HNO_3 or NaOH solutions. 0.1–4.0 g of TSAM or RSAM was placed to a 100 mL conical flask containing 10–100 mg L^{-1} of the target adsorbate. The mixture was agitated in a horizontal oscillator at 200 rpm at room temperature for a predetermined duration. Subsequently, the suspension was filtered, and the filtrate was analyzed to determine the residual concentration of the adsorbate. The removal efficiency (%) and amount adsorption capacity were calculated by the following equations:

$$\text{Removal efficiency}(\%) = \frac{C_0 - C_e}{C_0} \times 100\%$$

$$\text{Adsorption capacity}(q_e) = \frac{(C_0 - C_e) \times V}{m}$$

where q_e (mg g^{-1}) denotes the quantity of substance adsorbed at equilibrium. C_0 (mg L^{-1}) and C_e (mg L^{-1}) correspond to the initial and equilibrium concentrations of the solvent, respectively. The symbol V (L) signifies the volume of the solution, while m (g) indicates the mass of the adsorbent.

2.3.2 Adsorption models

2.3.2.1 Adsorption isotherm models. The adsorption isotherm model characterizes the equilibrium relationship between the adsorbate concentration in the liquid phase and the adsorbed amount on the solid phase, offering critical insights into the adsorption capacity of the adsorption materials. The experimental adsorption data were analyzed using three established isotherm models: the Langmuir, Freundlich, and Redlich–Peterson equations as follows:

$$\text{Langmuir model}: q_e = \frac{Q^0_{max} K_L C_e}{1 + K_L C_e}$$

$$\text{Freundlich model}: q_e = K_F C_e^n$$

$$\text{Redlich-Peterson model}: q_e = \frac{K_{RP} C_e}{1 + a_{RP} C_e^g}$$

where Q^0_{max} (mg g^{-1}) is the maximum saturated monolayer adsorption capacity of an adsorbent, C_e (mg L^{-1}) is the adsorbate concentration at equilibrium, q_e (mg g^{-1}) is the amount of adsorbate uptake at equilibrium, and K_L (L mg^{-1}) is a constant related to the affinity between an adsorbent and adsorbate, K_F (mg g^{-1}) (mg^{-1} L)$^{-n}$ is the Freundlich constant, and n (dimensionless) is the Freundlich intensity parameter, K_{RP} (L g^{-1}) and a_{RP} (mg L^{-1})$^{-g}$ are the Redlich-Peterson constants and g (dimensionless) is an exponent.

2.3.2.2 Adsorption kinetics models. The primary objective of adsorption kinetics studies is to probe the temporal evolution of substances on adsorbent surfaces during adsorption processes. This research aims to elucidate the rate at which substances

migrate from the solution phase to the adsorbent surface and identify the rate-limiting steps governing the adsorption mechanism. 3 widely used kinetic models pseudo-first-order (PFO), pseudo-second-order (PSO) and intra-particle diffusion model were used for this study, and the equations are as follows:

$$\text{PFO model}: \log(q_e - q_t) = -\frac{k_1}{2.303}t + \log(q_e)$$

$$\text{PSO model}: \frac{t}{q_t} = \left(\frac{1}{q_e}\right)t + \frac{1}{k_2 q_e^2}$$

$$\text{Intra-particle diffusion model}: q_t = k_p\sqrt{t} + C$$

where q_e and q_t are the amounts of adsorbate uptake per mass of adsorbent at equilibrium and at any time t (min), respectively, and k_1 (min^{-1}) is the rate constant of the PFO equation, k_2 ($g\ mg^{-1} \times min$) is the rate constant of the PSO equation, k_p ($mg\ g^{-1} \times min^{1/2}$) is the rate constant of the intra-particle diffusion model and C ($mg\ g^{-1}$) is a constant associated with the thickness of the boundary layer, where a higher value of C corresponds to a greater effect on the limiting boundary layer.

2.3.2.3 Desorption regeneration study. The reusability of an adsorbent is a crucial factor in ensuring sustainable and cost-effective industrial wastewater treatment. After the adsorption experiments, the adsorbent was separated *via* filtration for subsequent desorption and recyclability assessment. The spent adsorbent was subjected to elution using a 0.1 mol L^{-1} HCl solution for 30 minutes at room temperature to facilitate heavy metal desorption and adsorbent regeneration. The eluted adsorbent was then rinsed repeatedly with deionized water until the washing solution was neutral, followed by drying in an oven at 45 °C for 24 h. The regenerated adsorbent was subsequently reused in repeated adsorption tests, with the desorption process repeated identically for each subsequent cycle. The adsorption–desorption procedure was conducted over four or five cycles, and the adsorption capacity in each cycle was determined to evaluate reusability.

2.4 Adsorption experiments with actual wastewater

The actual wastewater samples were collected from tailings slurry of a copper flotation plant in Gansu Province. The plant employs a closed-circuit flowsheet consisting of one roughing, one scavenging, and three cleaning stages, with middlings sequentially returned. The collector used was sodium butyl xanthate, and the frother was terpenic oil. The pollutant content in actual wastewater is shown in Table 1. According to the <Emission standard of pollutants for copper, nickel, cobalt industry> (GB25466.1-2025),[47] the concentrations of Cd, Cu, Zn and chemical oxygen demand (COD) in wastewater exceeded the regulatory discharge limits. The wastewater requires proper purification treatment before authorized discharge. RSAM and TSAM were added into conical flasks containing 100 mL actual wastewater. The conical flasks were placed on a horizontal shaker (200 rpm) and agitated at room temperature.

Table 1 The components of actual wastewater

Components	Actual wastewater	Emission standard (GB25467-2010)
As ($mg\ L^{-1}$)	0.0425	0.5
Cd ($mg\ L^{-1}$)	0.405	0.1
Cu ($mg\ L^{-1}$)	0.57	0.2
Pb ($mg\ L^{-1}$)	0.0288	0.5
Zn ($mg\ L^{-1}$)	4.35	1.5
Cr ($mg\ L^{-1}$)	0.0047	—
Residual butyl xanthate ($mg\ L^{-1}$)	36.6	—
COD	187	100
pH	10.3	6–9

Subsequently, the mixture was filtered, and the filtrate were analyzed for residual pollutant concentrations.

3 Results and discussion

3.1 Characterization of TSAM and RSASM

The proximate and ultimate analysis were shown in Table 2. The main components of RSAM are ash and fixed carbon, the TSAM is composed of a large amount of ash and a small amount of fixed carbon. TSAM contains a large amount of total sulfur, metal sulfides can hydrolyze into alkaline substances in water. The ultimate analysis of RSAM showed that the C element was 51.58%.

Fig. 1 is the XRD analysis of TSAM and RSAM, both of two materials have similar compositions of calcium aluminates silicate ($CaAl_2Si_2O_8$) at 2θ angles of 20.8° and 26.6°. RSAM has fewer crystal phases and C elements exist in the form of amorphous carbons. RSAM contained a small amount of iron oxide (Fe_3O_4) at 2θ angles of 66.6°, which was produced during the high-temperature pyrolysis. The main crystalline phases of TSAM are calcium aluminates silicate ($CaAl_2Si_2O_8$), calcium sulfide (CaS) and iron sulfide.

Table 2 Proximate and ultimate analysis (air-dried basis)

	TSAM	RSAM
Proximate analysis (wt%)		
Moisture	0.11	2.17
Ash	72.18	48.42
Volatile	5.01	2.45
Fixed carbon	22.70	46.96
Total sulfur	18.40	1.31
Ultimate analysis (wt%)		
C	26.36	51.58
H	0.81	0.63
O	1.12	0.47
N	0.37	0.41
S	18.40	1.31
H/C	0.031	0.012
O/C	0.042	0.009

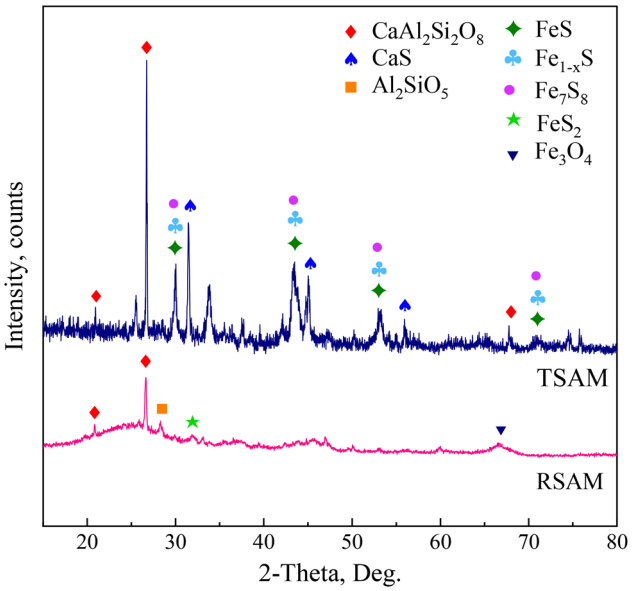

Fig. 1 XRD patterns of TSAM and RSAM.

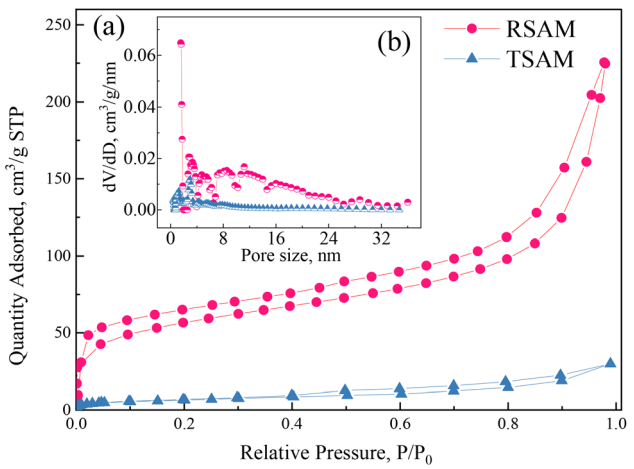

Fig. 2 N_2 adsorption/desorption isotherms (a) and pore size distribution (b).

The nitrogen adsorption/desorption isotherms and pore size distribution of RSAM and TSAM were shown in Fig. 2, and the related parameters calculated were displayed in Table 3. Both of RSAM and TSAM exhibit similar type H4 curves with hysteresis loops typically for mesopores according to the classification of IUPAC. This type occurs in solids containing narrow crack pores. From the nitrogen adsorption/desorption isotherms, RSAM exhibits a much larger equilibrium adsorption quantity than TSAM at any given relative pressure, indicating a substantially higher adsorption capacity.

Based on Fig. 2(a), both of RSAM and TSAM curves are type II isotherm, which represents the adsorption of monolayer-multilayer adsorption, implying the presence of combining macropores and mesopores. When $P/P_0 < 0.1$, the N_2 adsorption capacity of RSAM started to raise slowly, indicated that there are fewer micropores in RSAM. Both of RSAM and TSAM exhibit similar type H4 curves with hysteresis loops typically for mesopores according to the classification of IUPAC. This type occurs in solids containing narrow crack pores. Compare two nitrogen adsorption/desorption isotherm curves of RSAM and TSAM, the adsorption rate of RSAM is much higher than TSAM. In Fig. 2(b), the micropores distribution range of RSAM is narrow, mainly in 1.6 ~ 1.9 nm. The mesopores are mainly distribution in the range of 2 ~ 35 nm. The micropores distribution range of TSAM are mainly in 1 ~ 2 nm. The mesopores are mainly distribution in the range of 2 ~ 4 nm. Compare two pore size distribution curves of RSAM and TSAM, the pore volume of RSAM is larger than TSAM. RSAM has the larger BET surface area of 204 $m^2\ g^{-1}$ (Table 3), and larger pore volume of 0.314 cc g^{-1} with a smaller pore diameter of 6 nm.

As shown in Fig. 3(a) and (b), the TSAM has the fine-grained surface morphology with a small amount of large, smooth-surfaced particles mixed in. The two morphologies of TSAM were analyzed by EDS, point 1 for fine particles and point 2 for smooth large particles. Point 1 predominantly consists of minerals and negligible quantities of hydrocarbon. Main elements are carbon, calcium and sulfur. The carbon content exceeds 60%, combined with its morphology, it is speculated that the main components of point 2 are colloid and asphaltene, and Fe content of point 2 was significantly higher than that of point 1. SEM-EDS analysis of TSAM illustrates the inhomogeneous surface composition of this material. RSAM in Fig. 3(c) and (d) demonstrate distinct morphological characteristics from TSAM. The RSAM surface appears as uniform flocculent particles. These structures provide a large number of active adsorption sites for the removal of pollutants. The EDS point scan spectrum of RSAM is shown in Fig. 3(f). Point 3 and point 4 are similar in composition, with carbon, aluminum and silicon as the main elements. Detailed parameters of the SEM-EDS point scanning are summarized in Table 4.

To ensure the safety of using RSAM and TSAM in water treatment, leaching toxicity tests were carried out, the results are shown in Table 5. The leaching concentrations of all heavy

Table 3 Surface area and pore structure parameters

Samples	S_{BET}[a] ($m^2\ g^{-1}$)	S_{micro}[b] ($m^2\ g^{-1}$)	S_{meso}[c] ($m^2\ g^{-1}$)	V_{Total}[d] (cc g^{-1})	V_{micro}[e] (cc g^{-1})	D_p[f] (nm)
RSAM	204	42	162	0.314	0.034	6
TSAM	27	14	13	0.043	0.07	30

[a] BET surface area of materials. [b] Micropore surface area. [c] Mesopore surface are. [d] Total pore volume. [e] Micropore volume. [f] Average pore diameter.

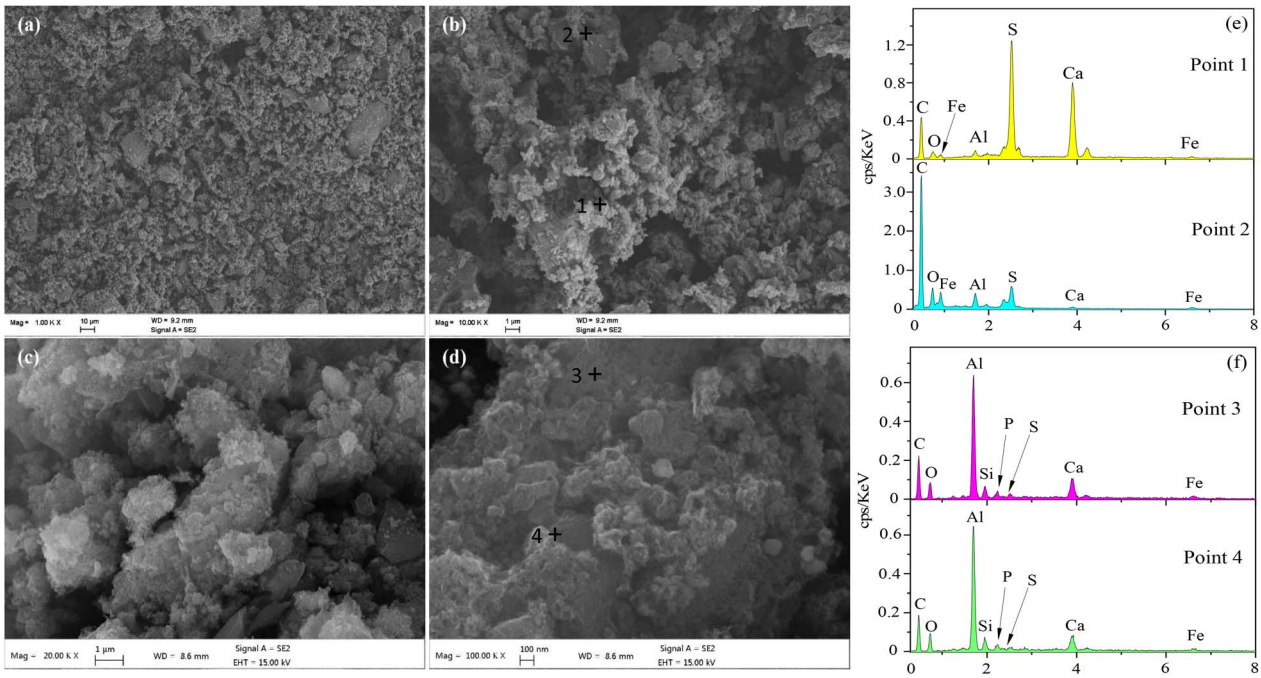

Fig. 3 SEM-EDS analysis of TSAM (a, and b: SEM, e: EDS) and RSAM (c, and d: SEM, f: EDS).

Table 4 EDS spectrum of TSAM and RSAM (wt%)

	TSAM		RSAM	
Elements	Point 1	Point 2	Point 3	Point 4
C	20.93	60.08	46.05	46.56
O	2.26	7.65	14.19	13.34
Al	0.75	3.3	23.53	21.03
Si	—	—	2.8	2.59
P	—	—	1.64	1.51
S	27.34	8.37	0.84	1.07
Ca	45.87	1.31	7.75	9.57
Fe	2.85	19.3	3.2	4.06

metal ion are below the limits of relevant standards for surface water discharges. Both adsorption materials leach more heavy metal ion in acidic environments. The raw materials utilized in the preparation of adsorbents contain a significant amount of organic matter and oil, it is necessary to test for volatile phenol and COD. No volatile phenol or petroleum were found in the leachate. At neutral pH, both materials meet emission standards for COD dissolved in water. RSAM and TSAM are safety for water treatment.

3.2 Study on the adsorption of butyl xanthate

3.2.1 Effect of dosages. Fig. 4 shows the effect of RSAM and TSAM dosages on the removal efficiency of butyl xanthate at different initial concentrations. As shown in Fig. 4(a), when the initial concentration was 40 mg L^{-1}, the removal efficiency of BX by RSAM increased with increasing dosage. When the dosage was less than 1 g L^{-1}, the removal efficiency by RSAM increased rapidly. The removal efficiency of BX could reach 99.30% at a dosage of 1.2 g L^{-1}. The removal efficiency of TSAM increased slowly with the increase of dosage. When the dosage of TSAM was 3.0 g L^{-1}, the removal efficiency remained stable, at which point the removal efficiency was 34.5%. The BX removed by RSAM was significantly higher than that removed by TSAM. The adsorption capacity of BX by RSAM was consistently higher than that by TSAM. Fig. 4(b) shows the effects of different doses on the removal efficiency of BX by TSAM and RSAM when the initial concentration of BX was 100 mg L^{-1}. The removal efficiency of BX by RSAM increased sharply with the increase of dosage, and the removal efficiency gradually stabilized when the dosage was 2.0 g, at which the removal efficiency reached 99.60%. The maximum removal efficiency of BX by TSAM was 12.93% when the dosage was 4.0 g L^{-1}. It can be seen that RSAM is much effective in removing BX.

3.2.2 Effect of adsorption time. Fig. 5 Effect of adsorption time on the BX removal efficiency of RSAM and TSAM. As shown in the figure, the removal efficiency and adsorption capacity of RSAM for BX increase with the increase of adsorption time. At

Table 5 Leaching toxicity of RSAM and TSAM (mg L^{-1})

Elements	RSAM	TSAM	Emission standard (GB 3838-2002 class IV water)
Cd^{2+}	ND	ND	0.05
Cu^{2+}	0.0194	0.0483	1.0
Zn^{2+}	0.0281	0.0730	1.0
Pb^{2+}	0.0158	0.0282	0.05
As^{2+}	ND	0.0002	0.1
Volatile phenol	ND	ND	0.01
Sulfide	0.0211	0.1097	0.5
COD	0.0300	0.0100	40

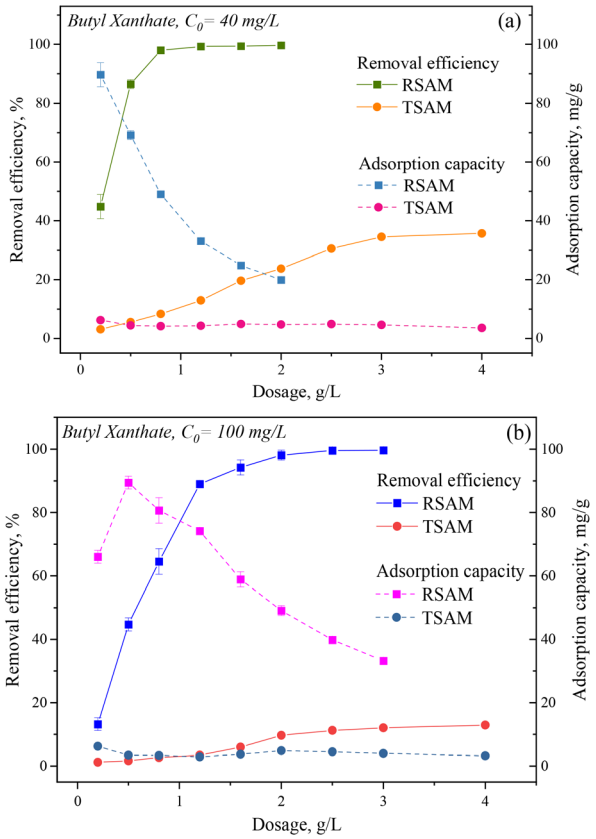

Fig. 4 Effect of dosages on BX removal efficiency at the initial concentration of 40 mg L^{-1} (a) and 100 mg L^{-1} (b).

45 minutes of adsorption time, the removal efficiency of RSAM for BX reaches its peak at 98.67 mg g^{-1}. The removal efficiency of BX by TSAM is minimally affected by adsorption time, with a maximum removal efficiency of 10.52%.

3.2.3 Effect of initial pH. The effect of initial pH on BX removal efficiency is shown in Fig. 6. The initial pH has no effect on the removal of BX by RSAM when the initial pH is below 9.5. There is little change in equilibrium pH and all equilibrium pH is blow 9.5 if the initial pH is below 9.5. The removal efficiency of BX begins to decrease with the increase of initial pH. The

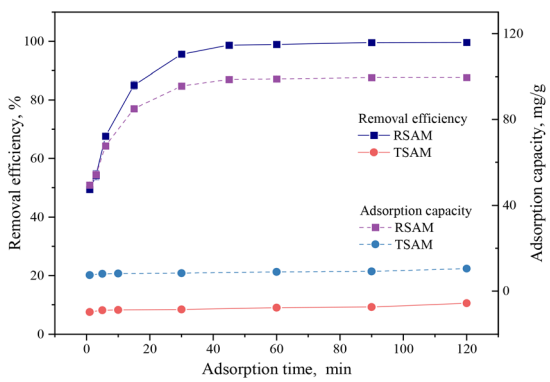

Fig. 5 Effect of adsorption time on BX removal efficiency.

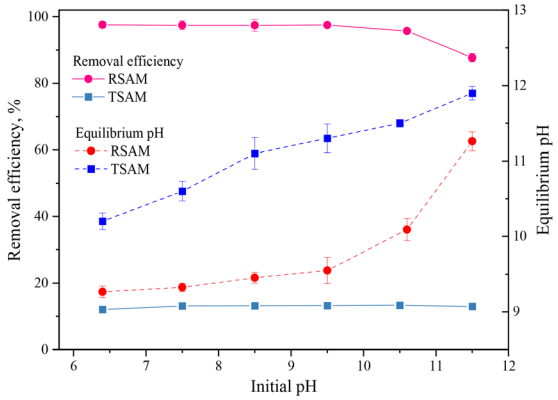

Fig. 6 Effect of initial pH on BX removal efficiency.

high alkaline pH has a significant negative impact on the removal of BX by RSAM. After the initial pH was greater than 9.5, the equilibrium pH increased substantially with the initial pH. When the equilibrium pH was 11.26, the removal efficiency of BX by RSAM decreased to 87.73%. The initial pH has little effect on the removal of BX by TSAM and the removal rate remains below 15%. Comparing the equilibrium pH curves of RSAM and TSAM, it can be seen that the equilibrium pH above 9.5 has negative effect on the removal of BX.

3.3 Adsorption isotherms and kinetic for butyl xanthate (BX)

The fitting curves for the Langmuir, Freundlich and Redlich-Peterson isotherm models of RSAM and TSAM for BX are demonstrated in Fig. S1, with the parameters detailed in Table S1. The adsorption isotherms of BX on RSAM and TSAM were best described Redlich-Peterson model, with nearly overlapping fitting curves and higher correlation coefficients (R^2 = 0.9928 and 0.9963, respectively) compared to the Langmuir and Freundlich models. The Freundlich and Redlich-Peterson model displayed nearly overlapping kinetic fitting curves. This confirms that the adsorption process follows a heterogeneous multilayer mechanism. The Freundlich intensity parameter $1/n$ values (0.28 for RSAM, 0.37 for TSAM) confirm favorable BX adsorption, as $0 < 1/n < 0.5$.

It is essential to evaluate the kinetic of the adsorption process in order to study the performance of RSAM and TSAM absorbing BX. The data obtained from kinetic models can be utilized to describe the mechanism of interaction between the RSAM or TSAM and butyl xanthate molecules. The curve fitting results and the parameters of the kinetic models are shown in the Fig. S2 and Table S2. The pseudo-first-order (PFO), pseudo-second-order (PSO) and intra-particle diffusion correlation coefficients (R^2) of TSAM for BX adsorption are 0.9973, 0.9887 and 0.9480, respectively. The PFO kinetic model was a more accurate description of the adsorption process between TSAM and butyl xanthate, which means that the adsorption of butyl xanthate by TSAM is a physical adsorption.[48]

The PFO, PSO and intra-particle diffusion correlation coefficients (R^2) of RSAM for BX adsorption are 0.7273, 0.8846 and 0.9943, respectively. The intra-particle diffusion model was

employed to establish the rate-controlling step of BX removal onto RSAM. The linear graph between q_t and $t^{0.5}$ didn't show the line passing through the origin as shown in Fig. S2(b), indicating that the intra-particle diffusion wasn't the only rate-controlling step for BX adsorption by RSAM.[49] Meanwhile, there are two linear steps occurred during the adsorption process. The first stage is external mass transfer or film diffusion. BX is transferred from the bulk phase to the surface of the adsorbent. The second stage is much slower than the first stage, because of the BX molecules diffuse into the pores of the adsorbent.[50] In the second stage, BX molecules diffuse to the pores of RSAM, and the slower adsorption process is due to the intra-particle diffusion.[51]

3.4 Study on the adsorption of Cd^{2+}, Cu^{2+} and Zn^{2+}

3.4.1 Adsorption characteristics of heavy metal ions. The effects of the two adsorption materials dosages on the removal of 3 heavy metal ions are shown in Fig. 7(a). With the increasing of adsorbent dosage, the removal efficiency of Cd^{2+}, Cu^{2+} and Zn^{2+} by both TSAM and RSAM increased. TSAM can effectively remove the 3 ions with a lower dosage compared to RSAM. When the dosage of TSAM was 1.0 g L^{-1}, the removal efficiency of Cd^{2+}, Cu^{2+} and Zn^{2+} achieved 99.31%, 99.93% and 97.15%. Meanwhile, the removal efficiency of 3 ions by RSAM was 40.95%, 44.63% and 25.81%. It is known from the effects of dosage on effluent pH in Fig. 7(b), with the increase of dosage, the effect of TSAM on effluent pH increased rapidly, while RSAM had little effect on effluent pH. When the dosage of TSAM was 1.0 g L^{-1}, the effluent pH was between 9 to 10, and 3 heavy metal ions were removed practically. It can be concluded that the removal of 3 heavy metal ions by TSAM is related to the rising of pH of aqueous solution.

The effect of initial pH on 3 ions removal efficiency were studied in the range of 2.0 to 9.0, which was shown in Fig. 7(c). With the increase of initial pH, the removal efficiency of heavy metal ions increased rapidly. For TSAM, when the initial pH reached 3, the removal efficiency of Cd^{2+}, Cu^{2+} and Zn^{2+} were 81.24%, 68.38% and 66.59%. When the pH reached 7, the removal efficiency of 3 ions was up to 97.90%, 99.93% and 98.96%. The heavy metal ions were removed effectively by TSAM. When the initial pH was 8, the removal efficiency of Cd^{2+}, Cu^{2+} and Zn^{2+} by RSAM were 52.17%, 69.15% and 43.73%, respectively. Theoretically, when the pH of solution is higher than 7, it is conducive to the removal of heavy metal ions.

The removal efficiency of initial concentration on the removal of 3 heavy metal ions is shown in Fig. 7(d). The removal efficiency of Cd^{2+}, Cu^{2+} and Zn^{2+} by RSAM decreased rapidly with the increase of initial concentration. While, the removal efficiency 3 ions by TSAM has been maintained above 99%. According to the experiments above, TSAM is more suitable for the removal of heavy metal ions compared with RSAM.

3.4.2 Adsorption isotherms and kinetic for Cd^{2+}, Cu^{2+} and Zn^{2+}. The adsorption isotherm fitting results of TSAM and RSAM for Cd^{2+}, Cu^{2+} and Zn^{2+} removal were shown in Fig. S3 and the parameters were shown in Table S3. The adsorption capacity (q_e) of TSAM and RSAM exhibited a positive correlation

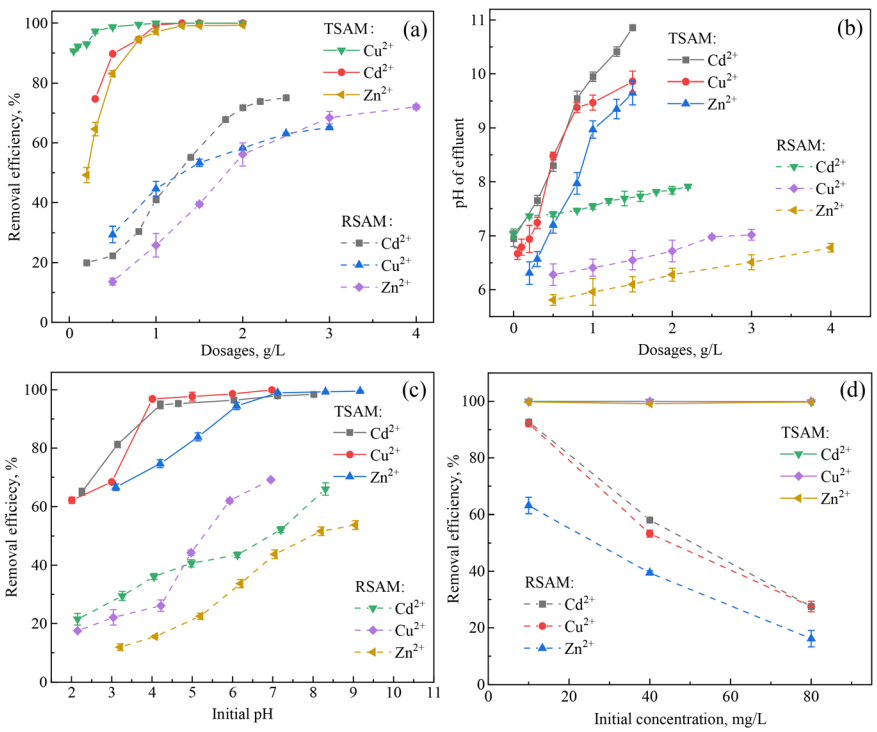

Fig. 7 (a) Effect of dosages on Cd^{2+}, Cu^{2+} and Zn^{2+} removal efficiency by TSAM and RSAM; (b) effect of dosages on effluent pH by TSAM and RSAM; (c) effect of initial concentration on Cd^{2+}, Cu^{2+} and Zn^{2+} removal efficiency by TSAM and RSAM; (d) effect of initial pH on Cd^{2+}, Cu^{2+} and Zn^{2+} removal efficiency by TSAM and RSAM.

with the initial concentrations of Cd^{2+}, Cu^{2+} and Zn^{2+}, which can be attributed to the enhanced mass transfer driving force at higher contaminant concentrations, thereby promoting their adsorption onto the adsorbent surface.[52,53] The q_e ultimately approached equilibrium due to the attainment of adsorption saturation, indicating the exhaustion of available active sites on the adsorbent surface. The adsorption behavior of TSAM and RSAM for Cd^{2+}, Cu^{2+} and Zn^{2+} were quantitatively analyzed using Langmuir, Freundlich and Redlich-Peterson isothermal models. The fitting parameters were shown in Supplementary Table S3. For the process of TSAM adsorbing Cd^{2+}, Cu^{2+} and Zn^{2+}, the correlation coefficients of Redlich-Peterson model exceeded 0.98, which was the highest among the 3 fitting models. The constants of R–P model K_{RP} and A_{RP} are larger than 1, and g is equal to 1, the eqn (n) transforms into the Freundlich isotherm. When g is larger than 1, the data is not explained by the R–P equation.[52] Therefore, the process of TSAM adsorbing Cd^{2+}, Cu^{2+} conform to Freundlich model, which is heterogeneous multi-layer adsorption. The adsorption behavior of TSAM adsorbing Zn^{2+} followed the Langmuir isotherm model, indicating a homogeneous monolayer adsorption process with maximum adsorption capacity of 100.01 mg g^{-1}. According to the parameters listed in Table S3, the adsorption process of RSAM for Cd^{2+}, Cu^{2+} conform to Redlich-Peterson model, indicating a hybrid adsorption mechanism combing both monolayer and heterogeneous surface interactions. The adsorption isotherm of Zn^{2+} onto RSAM demonstrated strict adherence to the Langmuir model ($R^2 = 0.96$). The maximum adsorption capacity of RSAM for Zn^{2+} was 23.12 mg g^{-1}.

The fitting results of pseudo-first-order and pseudo-second-order kinetic models of TSAM and RSAM adsorbing Cd^{2+}, Cu^{2+} and Zn^{2+} were shown in Fig. S4, and the parameters were shown in Table S4. The above experimental data achieved when the adsorption process reached equilibration. The pseudo-

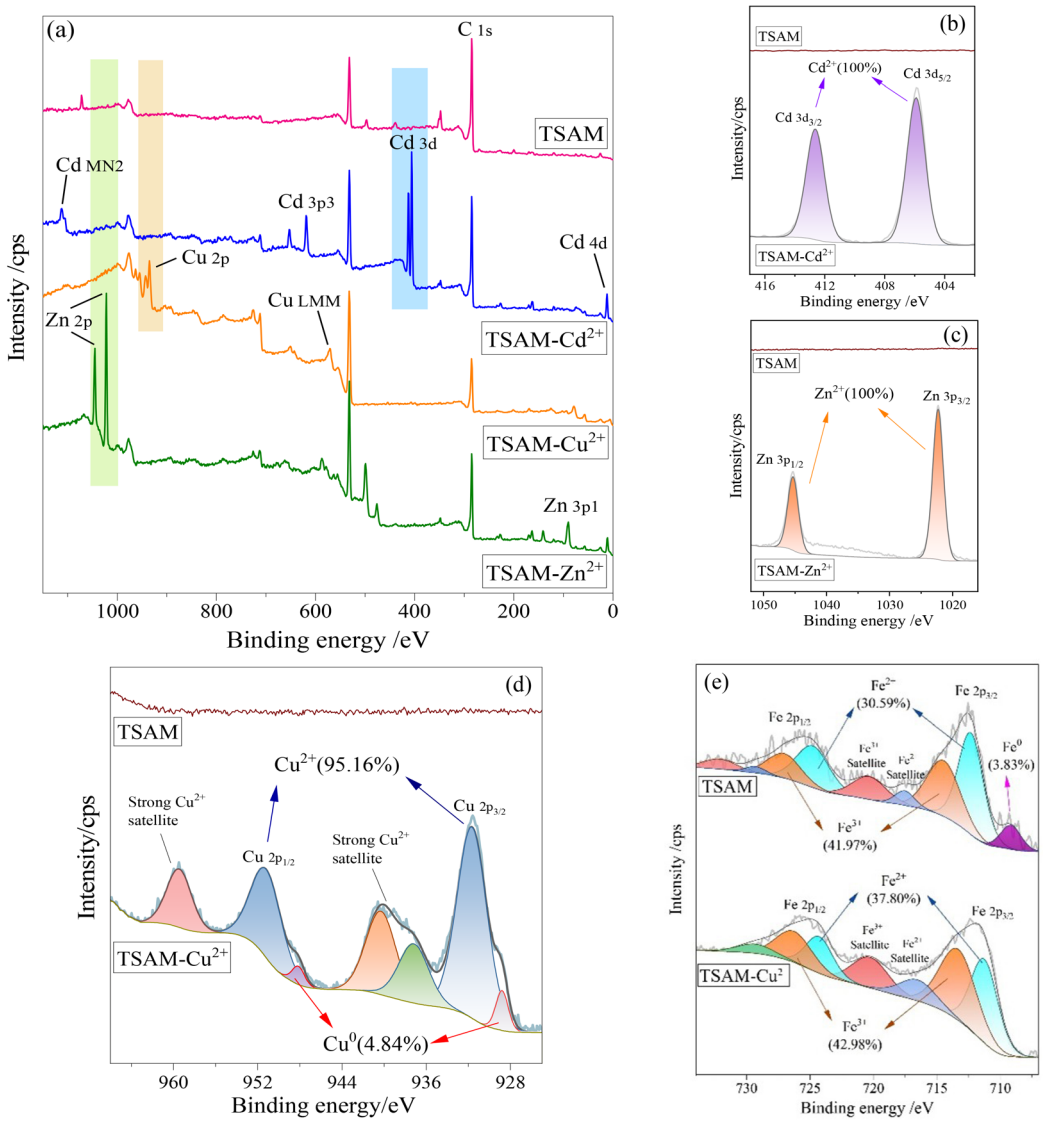

Fig. 8 XPS analyses of TSAM before and after adsorbing heavy metal ions. (a) Wide XPS spectrum; (b) Cd 3d spectrum; (c) Zn 3p spectrum; (d) Cu 2p spectrum; (e) Fe 2p spectrum of TSAM-Cu^{2+}.

second-order kinetic model demonstrates excellent correlation with the adsorption data for TSAM, as evidenced by correlation coefficients (R^2) of 0.99, 0.97 and 0.99, respectively. The equilibrium adsorption capacities of 3 ions are 42.51 mg g^{-1}, 89.92 mg g^{-1} and 65.29 mg g^{-1}. Consistent with the pseudo-second-order kinetic results, the adsorption of TSAM adsorbing Cd^{2+}, Cu^{2+} and Zn^{2+} proceeds *via* chemisorption processes that involve electron transfer or shared electron pairs between the adsorbate and surface active sites. According to the correlation coefficient (R^2) of the fitting results, the adsorption process of 3 heavy metal ions by RSAM follows pseudo-first-order kinetics, with R^2 higher than 0.99. The fitting results conform to the pseudo-first-order adsorption kinetics model, indicating that the rate of the adsorption process is mainly controlled by physical adsorption or diffusion steps.

3.4.3 Adsorption mechanism. Given the demonstrated efficacy of TSAM in heavy metal ions removal, X-ray photoelectron spectroscopy (XPS) was selectively employed to characterize the adsorption mechanism specifically for Cd^{2+}, Cu^{2+} and Zn^{2+}. The spectrums were shown in Fig. 8. Fig. 8(a) highlighted the alterations in chemical composition and valence states of TSAM before and after the adsorption of Cd^{2+}, Cu^{2+} and Zn^{2+}. As demonstrated in Fig. 8(b) and (c), the high-resolution spectrum provide conclusive evidence for the surface adsorption of Cd^{2+} and Zn^{2+} by TSAM. Fig. 8(d) of Cu 2p high-resolution spectrum revealed characteristic Cu 2p3/2 and Cu 2p1/2 peaks at 931.81 eV and 951.54 eV, respectively, which are diagnostic of Cu(II) species. Additionally, satellite features observed at 939.97 eV and 959.60 eV further confirmed the presence of Cu(II) through their distinctive shake-up transitions. The spectrum also exhibited minor components at 928.83 eV (Cu 2p3/2) and 948.14 eV (Cu 2p1/2), corresponding to metallic Cu(0), with quantitative analysis indicating this species accounts for 4.84% of the total copper content. As illustrated in Fig. 8(e), the Fe 2p XPS spectrum revealed that the relative content of Fe^0, Fe^{2+}, and Fe^{3+} on the TSAM surface were 3.83%, 30.59% and 41.97%, respectively. After the Cu^{2+} adsorption, the content of Fe^{2+} and Fe^{3+} increased to 37.80% and 42.98%, while the Fe^0 species completely disappeared. This observation, combined with the analysis of Cu 2p, provides compelling evidence for a reduction reaction between iron species and copper ions. The possible chemical reaction can be represented as follows:

$$2Fe^{3+} + Fe \rightarrow 3Fe^{2+}$$

$$2Fe^{2+} + Cu^{2+} \rightarrow Cu^0 + 2Fe^{3+}$$

The simulated wastewater was used for the adsorption experiments of TSAM and RSAM. The simulated wastewater

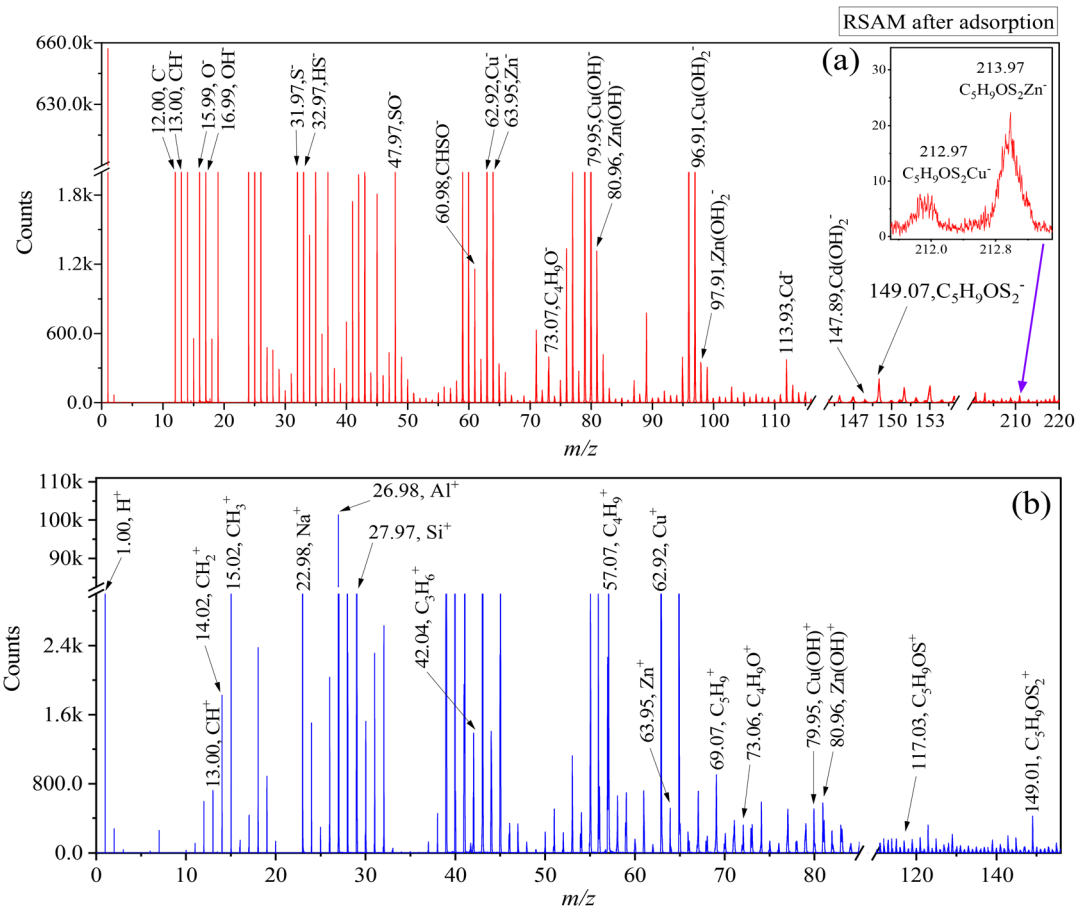

Fig. 9 ToF-SIMS analysis of RSAM after simulated wastewater treatment (a) the negative ion. (b) The positive ion.

contained Cu^{2+}, Cd^{2+}, Zn^{2+}, and butyl xanthate at concentrations corresponding to those in actual wastewater (see in Table 1). The solvent used for the preparation of simulated wastewater was distilled water, and the pH of solution is 5.5. The RSAM and TSAM samples after adsorption treatment were characterized by ToF-SIMS analysis to investigate their pollutant removal mechanisms in complex aqueous environments. The analysis spectrum results were shown in Fig. 9.

In the negative ion spectrum, multiple heavy metals, BX, and related compounds were detected on the surface of RSAM after adsorption. At the *m*/*z* of 60.98 and 73.07, the ion fragments $CHSO^-$ and $C_4H_9O^-$ of BX were identified, while at the presence of the xanthate negative ion $C_5H_9OS_2^-$ at the *m*/*z* 149.07 confirmed xanthate adsorption on the surface of RSAM. Minor peaks corresponding to $C_5H_9OS_2Cu^-$ and $C_5H_9OS_2Zn^-$ were observed at *m*/*z* 212.97 and 213.97, indicating the formation of trace heavy metal-butyl xanthate complexes adsorbed on the RSMA surface. At *m*/*z* 79.95 and 80.96, $Cu(OH)^-$ and $Zn(OH)^-$ were detected, which are ionic fragments of $Cu(OH)_2^-$ and $Zn(OH)_2^-$. Meanwhile, at *m*/*z* 96.91, 97.91, and 148.89, $Cu(OH)_2^-$, $Zn(OH)_2^-$, $Cd(OH)_2^-$ were found. In the positive ion spectrum, Cu^+ and Zn^+ ion fragments were observed at *m*/*z* of 62.92 and 63.95, respectively. $Cu(OH)_2^+$ and $Zn(OH)_2^+$ ion fragments were detected at mass-to-charge ratios of 79.95 and 80.96, respectively. Comprehensive spectrum analysis demonstrated that Cd^{2+}, Cu^{2+}, and Zn^{2+} were predominantly adsorbed on the RSAM surface by two distinct mechanisms: (i) precipitation as metal-butyl xanthate complexes and (ii) formation of metal hydroxide precipitates. In the negative ion spectrum, multiple heavy metals, BX, and related compounds were detected on the surface of RSAM after adsorption. At the *m*/*z* of 60.98 and 73.07, the ion fragments $CHSO^-$ and $C_4H_9O^-$ of BX were identified, while at the presence of the xanthate negative ion $C_5H_9OS_2^-$ at the *m*/*z* 149.07 confirmed xanthate adsorption on the surface of RSAM. Minor peaks corresponding to $C_5H_9OS_2Cu^-$ and $C_5H_9OS_2Zn^-$ were observed at *m*/*z* 212.97 and 213.97, indicating the formation of trace heavy metal-butyl xanthate complexes adsorbed on the RSMA surface. At *m*/*z* 79.95 and 80.96, $Cu(OH)^-$ and $Zn(OH)^-$ were detected, which are ionic fragments of $Cu(OH)_2^-$ and $Zn(OH)_2^-$. Meanwhile, at *m*/*z* 96.91, 97.91, and 148.89, $Cu(OH)_2^-$, $Zn(OH)_2^-$, $Cd(OH)_2^-$ were found. In the positive ion spectrum, Cu^+ and Zn^+ ion fragments were observed at *m*/*z* of 62.92 and 63.95, respectively. $Cu(OH)_2^+$ and $Zn(OH)_2^+$ ion fragments were detected at mass-to-charge ratios of 79.95 and 80.96, respectively. Comprehensive spectrum analysis demonstrated that Cd^{2+}, Cu^{2+}, and Zn^{2+} were

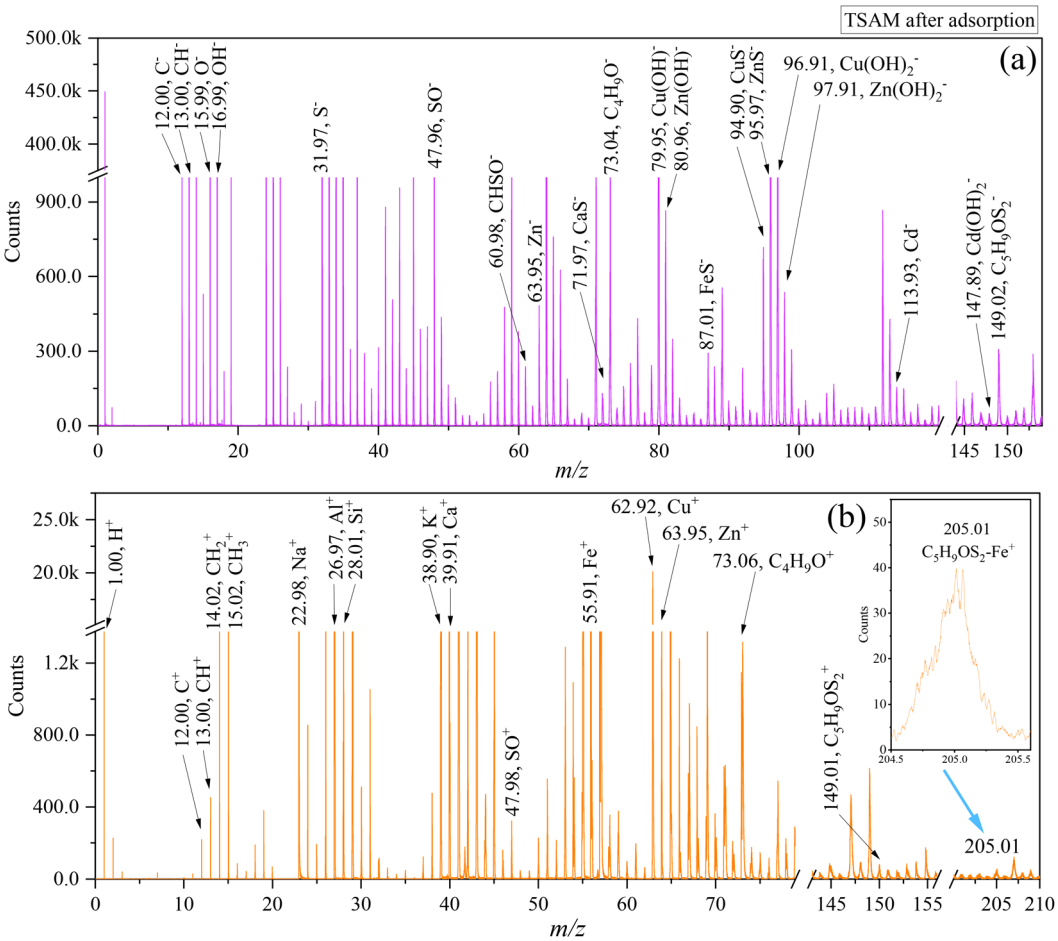

Fig. 10 ToF-SIMS analysis of TSAM after simulated wastewater treatment. (a) The negative ion. (b) The positive ion.

predominantly adsorbed on the RSAM surface by two distinct mechanisms: (i) precipitation as metal-butyl xanthate complexes and (ii) formation of metal hydroxide precipitates.

The ToF-SIMS analysis presented in Fig. 10(a) reveals that the treated TSAM retains a considerable concentration of metal sulfides, as indicated at *m*/*z* 71.97 corresponding to CaS and *m*/*z* 87.01 corresponding to FeS. Notably, the emergence of distinct ion fragments at *m*/*z* 94.90 and 95.97, corresponding to copper sulfide and zinc sulfide species respectively, provides definitive spectroscopic evidence for the formation of these metal sulfides. These findings demonstrate that copper and zinc ions participate in sulfidation reactions on the surface of the TSAM. Further analysis reveals characteristic peaks corresponding to metal hydroxide species, with *m*/*z* 79.95 representing $Cu(OH)^-$, 80.96 corresponding to $Zn(OH)^-$, 96.91 assigned to $Cu(OH)_2^-$, and 97.91 identified as $Zn(OH)_2^-$. These findings demonstrate that copper and zinc ions undergo additional immobilization through hydroxide precipitation on TSAM surface. The characteristic $Cd(OH)_2^-$ peak at *m*/*z* 147.89 confirms cadmium follows similar removal pathways. These findings demonstrate heavy metal removal occurs through two primary mechanisms: sulfide and hydroxide precipitation. Fig. 10(b) reveals characteristic xanthate ion fragments at *m*/*z* 60.98 and 149.02, demonstrating the adsorption of butyl xanthate on the TSAM surface. The significantly enhanced signals of Cu^+ and Zn^+ provide conclusive evidence for the exceptional removal efficiency of the TSAM toward heavy metal elements including Cu, Zn, and Cd.

Fig. S5 presents the TOF-SIMS negative fine spectra of TSAM before and after simulated wastewater adsorption treatment. Comparative analysis of spectra (a) and (b) reveals the emergence of distinct peaks corresponding to $Cu(OH)_2^-$ (*m*/*z* 96.91), $Zn(OH)_2^-$ (*m*/*z* 97.91), and $Cd(OH)_2^-$ (*m*/*z* 147.89) species post-adsorption. The sharp and intense peaks confirm that TSAM adsorbs heavy metal ions through hydroxide precipitation. Furthermore, as evidenced in Fig. 10(c), the detection of CuS^- and ZnS^- species on the post-adsorption TSAM surface indicates concurrent sulfide formation during the copper and zinc adsorption processes. The corresponding chemical reactions proceed as follows:

$$M^{2+} + OH^- \rightarrow M(OH)_2$$

$$M^{2+} + S^{2-} \rightarrow MS$$

3.5 Desorption and reusability performance

Reusability represents a critical consideration in the development of effective adsorbent for the treatment of industrial wastewater. Five or four adsorption–desorption rounds of cycle were repeated, with the results illustrated in Fig. 11. As shown in Fig. 11(a), the equilibrium adsorption capacity(q_e) of TSAM for Cd^{2+}, Cu^{2+} and Zn^{2+} decreased with increasing of cycle times. After 5 cycles, the q_e of TSAM for Cd^{2+}, Cu^{2+} and Zn^{2+} exhibited reductions of 27.61% (11.34 g), 24.28% (25.28 g) and 36.04% (17.08 g), respectively. The decline in adsorption capacity could result from either mass loss induced by mechanical agitation and collisions during desorption or the blocking of active adsorption sites. As the number of cycles increases, TSAM demonstrate significant potential as practical adsorbents for heavy metal ions wastewater treatment. Fig. 11(b) shows that q_e of RSAM for Cd^{2+}, Cu^{2+} and Zn^{2+} decreased by 48.01%, 54.00% and 50.15%, respectively. Given the limited adsorption capacity of RSAM for heavy metal ions, RSAM exhibits negligible affinity for relevant wastewater treatment.

3.6 Testing with actual wastewater

The experimental results of pollutant removal from actual wastewater using a mixed adsorbent are presented in Fig. 12. The ratio of the mixed adsorbent is TSAM : RSAM = 1 : 1. Fig. 12(a) shows the effect of mixed adsorbent dosage on the pollutant removal efficiency. At a dosage of 3 g L^{-1}, the mixed adsorbent reached maximum removal efficiencies for Cd, Cu, and BX, with efficiencies of 96.82%, 97.55% and 99.41%, respectively. Further increasing the dosage to 5 g L^{-1} resulted in removal efficiency of 83.06% for Zn and 33.60% for COD. Additionally, the mixed adsorbent contributed to a slight reduction in effluent pH. Fig. 12 shows the effect of treatment time on the pollutant removal efficiency. At a treatment time of 60 min, the mixed adsorbent achieved optimal pollutant removal efficiency, with removal efficiencies exceeding 96% for Cd, Cu and BX, while reaching 81.35% for Zn and 32.47% for

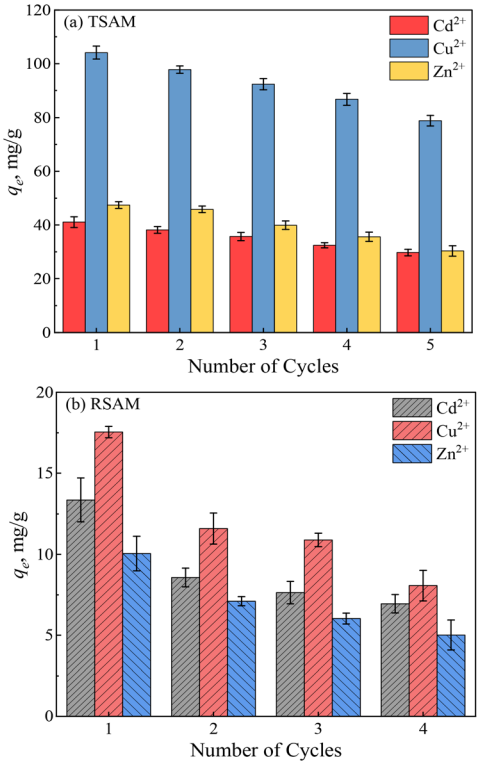

Fig. 11 Adsorption–desorption cycles for Cd^{2+}, Cu^{2+} and Zn^{2+} on TSAM (a) and RSAM (b). (An adsorbent amount of 2g L^{-1} and an adsorbate concentration 200 mg L^{-1} for Cd^{2+}, 300 mg L^{-1} for Cu^{2+} and 200 mg L^{-1} for Zn^{2+} at pH 7 were used; the desorption solvents used were 0.1 mol L^{-1} HCl.)

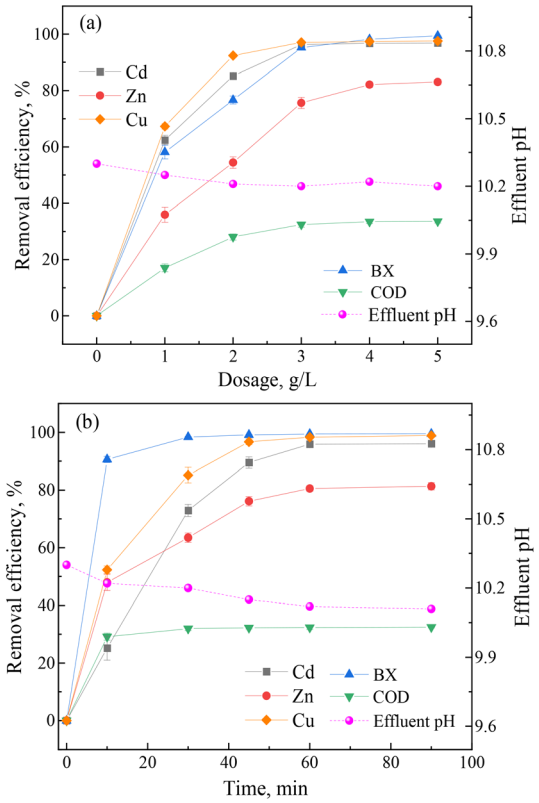

Fig. 12 Actual wastewater removal experiment by mixed adsorbent (a) dosage, (b) treatment time.

COD. The mixed adsorbent exhibited a COD removal efficiency of only 32.47%, primarily attributed to its selective adsorption characteristics. Mixed adsorbent effectively removes BX-derived COD fractions but shows limited efficacy for COD from other sources such as organic matters, nitrite, ferrous ions and other component in the wastewater. The mixed adsorbent composed of TSAM and RSAM demonstrated effective performance in treating actual mineral processing wastewater, showing significant potential for practical applications in industrial sector.

Fig. 13 illustrates the integrated research concept of this study, which proposes a sustainable, resource-recovery strategy for the treatment of refinery and tank bottom oily sludge. The process begins with the pyrolysis of both sludge types, achieving substantial sludge reduction while simultaneously recovering valuable oil and flammable gases. Crucially, the solid pyrolysis residue is valorized into functional adsorption materials—specifically, refinery sludge adsorption material (RSAM) and tank sludge adsorption material (TSAM)—thereby realizing the secondary utilization of pyrolysis residue. These materials are then applied in the adsorptive treatment of actual sulfide mineral flotation wastewater, demonstrating targeted removal capabilities: RSAM effectively adsorbs the organic collector butyl xanthate ($C_4H_9OCSSNa$), whereas TSAM exhibits a high affinity for heavy metal ions (Cu^{2+}, Cd^{2+}, and Zn^{2+}). This step embodies a "waste-treating-waste" approach, utilizing sludge-derived adsorbents to remediate another complex industrial effluent. Furthermore, the schematic implies an investigation into the underlying adsorption mechanisms for both pollutant types. Overall, this work establishes a closed-loop pathway that combines sludge reduction, resource recovery (oil and gas), pyrolysis residue valorization into functional materials, and the effective application of those materials in wastewater treatment, thereby addressing multiple environmental challenges within a unified framework.

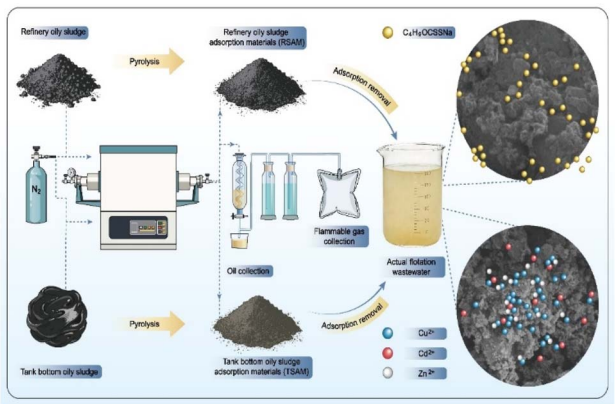

Fig. 13 Schematic diagram of the joint removal mechanisms of TSAM and RSAM.

4 Conclusions

This study demonstrates a sustainable and efficient approach to transforming hazardous oily sludge into functional adsorbents for the integrated treatment of mineral processing wastewater. The research highlights the distinct structural and functional characteristics of TSAM and RSAM, where RSAM, with its superior porosity and carbon-rich matrix, is optimized for the capture of organic collectors, whereas TSAM, enriched with active mineral phases, serves as an effective medium for heavy metal immobilization. The investigation reveals that the removal mechanisms are fundamentally different: RSAM relies on physical interactions, including pore filling and hydrophobicity, while TSAM facilitates chemical remediation through joint precipitation, surface complexation, and ion exchange, further supported by its inherent alkaline-buffering capacity. Furthermore, the successful treatment of actual tailings wastewater confirms that these sludge-derived materials can robustly handle complex industrial matrices, ensuring that multiple pollutants are reduced to safe discharge levels without secondary pollution risks. Ultimately, this "waste-treating-waste" strategy not only provides a cost-effective alternative to commercial adsorbents but also offers a viable pathway for the high-value valorization of petroleum waste, aligning with the goals of environmental remediation and circular economy.

Author contributions

Peng Fu: investigation, calculation, visualization, original draft. Huifen Yang: supervision, conceptualization, resources, data curation, review and editing. Jingwen Zhao: visualization, calculation.

Conflicts of interest

There are no conflicts to declare.

Data availability

The data that support the findings of this study are available from the corresponding author upon reasonable request.

Supplementary information (SI): contains 5 supplementary figures (Fig. S1–S5) illustrating the adsorption kinetics, isotherms, and ToF-SIMS characterization results of TSAM and RSAM, along with 4 supplementary tables (Tables S1–S4) summarizing the fitted parameters of the adsorption models. See DOI: https://doi.org/10.1039/d6ra00534a.

Acknowledgements

This study was supported by the National Key research and Development Program of China (2019YFC1803503), the Scientific Research support funds in Inner Mongolia (0303052503) and 2023 Inner Mongolia high-level talent research support program (0701012405).

References

1 National Agency of Petroleum, Natural Gas and Biofuels (ANP), Oil, Natural Gas and Biofuels Statistical Yearbook, 2010, Brasília, Brazil.
2 Q. Li, Y. Gao, G. Ji, C. Chen and A. Li, *Can. J. Chem. Eng.*, 2019, **98**, 465–474.
3 W. X. Chen H, H. Liang, B. Chen, Y. Liu, Z. Ma and Z. Wang, *Environ. Pollut.*, 2024, **344**, 123245.
4 J. Li, F. Lin, K. Li, F. Zheng, B. Yan, L. Che, W. Tian, G. Chen and K. Yoshikawa, *J. Hazard Mater.*, 2021, **406**, 124706.
5 W. Ma, Z. Li, H. Yang and P. Fu, *S. Afr. J. Chem. Eng.*, 2020, **34**, 82–89.
6 F. Li, Y. Zhang, S. Wang, G. Li, X. Yue, D. Zhong, C. Chen and K. Shen, *Chem. Eng. J.*, 2020, **385**, 123946.
7 C. L. Goh, S. Sethupathi, M. J. Bashir and W. Ahmed, *J. Environ. Manag.*, 2019, **237**, 281–288.
8 F. Meng, Z. Gong, Z. Wang, P. Fang and X. Li, *Fuel*, 2019, **251**, 562–571.
9 Z. Gong, F. Meng, Z. Wang, P. Fang, X. Li, L. Liu and H. Zhang, *Energy Fuels*, 2019, **33**, 10056–10065.
10 Q. Zhang, H. Yang, S. Guo, Q. Sun, G. Zhang and X. Li, *Groundw. Sustain. Dev.*, 2022, **18**, 100799.
11 T. Boualem, A. Debab, A. M. de Yuso and M. T. Izquierdo, *J. Environ. Manag.*, 2014, **140**, 145–151.
12 P. Devi and A. K. Saroha, *Sci. Total Environ.*, 2017, **578**, 16–33.
13 S. Singh, V. Kumar, D. S. Dhanjal, S. Datta, D. Bhatia, J. Dhiman, J. Samuel, R. Prasad and J. Singh, *J. Clean. Prod.*, 2020, **269**, 122259.
14 X. Du, D. Tian, Z. Yin and M. Chen, *Water Supply*, 2022, **22**, 8625–8636.
15 Y. Zhou, Y. Liu, L. Feng, Y. Xu, Z. Du and L. Zhang, *RSC Adv.*, 2020, **10**, 14510–14519.
16 L. Mao, M. Wu, S. Zhu, X. Wang, J. Zhang and Y. Qin, *Sustainability*, 2024, 16.
17 J. Chen, X. Dong, S. Cao, L. Zhu, Z. Song, J. Jin and H. Yang, *Desalination Water Treat.*, 2022, **249**, 61–73.
18 World Health Organization (WHO), Guidelines for drinking-water quality, fourth edition, Geneva Switerland.
19 R. Shrestha, S. Ban, S. Devkota, S. Sharma, R. Joshi, A. P. Tiwari, H. Y. Kim and M. K. Joshi, *J. Environ. Chem. Eng.*, 2021, **9**, 105688.
20 W. S. Chai, J. Y. Cheun, P. S. Kumar, M. Mubashir, Z. Majeed, F. Banat, S. H. Ho and P. L. Show, *J. Clean. Prod.*, 2021, **296**, 126589.
21 P. Saravanan, V. Saravanan, R. Rajeshkannan, G. Arnica, M. Rajasimman, G. Baskar and A. Pugazhendhi, *Environ. Res.*, 2024, **258**, 119440.
22 L. Joseph, B. M. Jun, J. R. V. Flora, C. M. Park and Y. Yoon, *Chemosphere*, 2019, **229**, 142–159.
23 A. A. Alcaine, C. Schulz, J. Bundschuh, G. Jacks, R. Thunvik, J. P. Gustafsson, C. M. Mörth, O. Sracek, A. Ahmad and P. Bhattacharya, *Sci. Total Environ.*, 2020, **715**, 136671.
24 J. P. Vareda, A. J. M. Valente and L. Durães, *J. Environ. Manag.*, 2019, **246**, 101–118.
25 Q. Huang, X. Li, S. Ren and W. Luo, *Colloids Surf., A*, 2019, **580**, 123723.
26 Y. Zheng, F. Yuan, D. Gao, L. Liu, L. Wang and X. Hu, *Mater. Res. Bull.*, 2023, **158**, 112080.
27 J. Yang, R. Huang, Y. Cao, H. Wang, A. Ivanets and C. Wang, *Environ. Sci. Pollut. Res.*, 2022, **29**, 75651–75663.
28 I. Muzinda and N. Schreithofer, *Miner. Eng.*, 2018, **125**, 34–41.
29 M. H. M. Noor and N. Ngadi, *J. Water Proc. Eng.*, 2024, **64**, 105696.
30 A. Pohl, *Water, Air, Soil Pollut.*, 2020, **231**, 503.
31 Z. Wang, Z. Tan, H. Li, S. Yuan, Y. Zhang and Y. Dong, *J. Clean. Prod.*, 2022, **339**, 130746.
32 S. A. Razzak, M. O. Faruque, Z. Alsheikh, L. Alsheikhmohamad, D. Alkuroud, A. Alfayez, S. M. Z. Hossain and M. M. Hossain, *Environ. Adv.*, 2022, **7**, 100168.
33 M. Jiang, M. Zhang, L. Wang, Y. Fei, S. Wang, A. Nunez-Delgado, A. Bokhari, M. Race, A. Khataee and J. J. Klemeš, *Chem. Eng. J.*, 2022, **431**, 134104.
34 A. de Barros Lima, I. B. A. Falconi, J. A. S. Tenorio and M. d. P. G. Baltazar, *J. Photochem. Photobiol., A*, 2023, **441**, 114678.
35 P. Fu, G. Li, X. Wu, X. Lin and B. Lei, *R. Soc. Open Sci.*, 2019, **6**, 190123.
36 S. Hube, M. Eskafi, K. F. Hrafnkelsdóttir, B. Bjarnadóttir, M. Á. Bjarnadóttir, S. Axelsdóttir and B. Wu, *Sci. Total Environ.*, 2020, **710**, 136375.
37 D. Ankoliya, A. Mudgal, M. K. Sinha, P. Davies, E. Licon, R. R. Alegre, V. Patel and J. Patel, *J. Clean. Prod.*, 2021, **319**, 128686.
38 L. Chai, Q. Li, Q. Wang and X. Yan, *Environ. Sci. Pollut. Res.*, 2018, **25**, 17250–17267.
39 Y. Dong, H. Lin, Q. Liu and H. Huo, *J. Cent. S. Univ.*, 2014, **21**, 3580–3587.

40 C. Boahen, S. Wiafe, F. Owusu and L. Bian, *Sustain. Environ.*, 2023, **9**, 2152590.
41 T. P. Fato, D. W. Li, L. J. Zhao, K. Qiu and Y. T. Long, *ACS Omega*, 2019, **4**, 7543–7549.
42 J. C. Zheng, H. M. Feng, M. H. W. Lam, P. K. S. Lam, Y. W. Ding and H. Q. Yu, *J. Hazard Mater.*, 2009, **171**, 780–785.
43 Y. Hou, K. Cheng, Z. Li, X. Ma, Y. Wei, L. Zhang and Y. Wang, *PLoS One*, 2015, **10**, e0140962.
44 M. A. R. Hamed and M. A. Abdallah, *J. Ecol. Eng.*, 2024, **25**, 111–118.
45 P. Fu, H. Yang, Q. Zhang and X. Li, *Int. J. Environ. Sci. Technol.*, 2022, **20**, 5035–5042.
46 H. Yang, Z. Li, P. Fu and G. Zhang, *Environ. Pollut.*, 2019, **249**, 843–850.
47 Ministry of Ecology and Environment, State Administration for Market Regulation, Emission Standard of Air Pollutants for Lead and Zinc Industry (Part 1) Standard Number: GB 25466.1—2025, Standards Press of China, Beijing, China, 2025.
48 T. C. Suyanne Angie Lunelli Bachmann and L. Amaral Féris, *Sci. Total Environ.*, 2021, **767**, 144229.
49 S. J. Fang Wei, C. Yao, T. Wang, S. Zhu, Y. Ma, H. Qiao, L. Shan, R. Wang, X. Lian, X. Tong, Li Yan, Q. Zhao and W. Song, *Molecules*, 2023, **28**, 114426.
50 B. Kumari, R. K. Tiwary and M. Yadav, *Mater. Chem. Phys.*, 2022, **290**, 126457.
51 A. E. Ofomaja, *Bioresour. Technol.*, 2010, **101**, 5868–5876.
52 H. N. Tran, S. J. You, A. Hosseini-Bandegharaei and H. P. Chao, *Water Res.*, 2017, **120**, 88–116.
53 T. E. Akinola, P. L. B. Prado and M. Wang, *Appl. Energy*, 2022, **317**, 119156.